

Numerical Simulation of the Influence of Electrode Shrinkage Cavity on ESR Process of IN718 Alloy

Wang Zixing^{1,2}, Li Qing², Wang Lei¹

¹ Key Laboratory for Anisotropy and Texture of Materials (Ministry of Education), Northeastern University, Shenyang 110819, China;

² Research Institute, Baoshan Iron & Steel Co., Ltd, Shanghai 201900, China

Abstract: Numerical simulation and analysis of the influence of electrode shrinkage cavity on electroslag remelting (ESR) process of IN718 alloy ingot with a diameter of 430 mm were carried out using the self-developed ESR process model. Electromagnetic fields of ESR system were simulated by a specially designed shrinkage cavity with different shapes and sizes in the electrode. The results show that the contacting area changes between the electrode and the slag owing to the cavity, which plays a predominant role in the distribution of the Joule heat and electromagnetic force in the slag, while the effect of axial dimension change of the shrinkage cavity is negligible. Constant melt rate ESR processes were simulated for different radius cavity situations. It is shown that, at a constant melt rate, the shrinkage cavity has no effect on the ESR process as its radius is less than 0.025 m, and only a small influence on the slag flow when the radius reaches 0.05 m. As the radius increases over 0.05 m, an increasingly evident influence on the slag zone appears via the weakened center downward flow and the increased temperature. Nevertheless, the cavity has no obvious influence on the ingot including the melt pool and mush zone. There is a nonlinear relation between the shrinkage cavity radius and the ESR melting parameters such as current and power, and the critical value of the radius is approximately 0.05 m. Below the critical value, faint or even no change in the parameters appears, while, above the value, the parameters of power and current increase rapidly in an approximately linear manner. From the standpoint of process control stability, the shrinkage cavity radius should be controlled below 0.05 m.

Key words: electroslag remelting; numerical simulation; electrode shrinkage cavity

Electroslag remelting (ESR) is one of the most important remelting processes, which has been widely used to produce high quality special steels and superalloys. ESR process research has long been known as a trial-and-error approach, owing to the complex process mechanism including multiple physical phenomena and interactions, phase transformations, and simultaneous chemical reactions. Fortunately, there is an alternative approach of numerical simulation for ESR research. ESR modelling and simulation has been profoundly developed over the last 4 decades, covering many aspects of physical processes, including electromagnetic field, fluid flow, heat transfer, mass transmission, electrode melting and dropping, ingot solidification, slag/metal interface phenomenon, solidification structure parameters, ingot element distribution,

etc.^[1-10]. With a systematically formulated ESR model, the ESR process can be simulated to optimize process parameters such as melt rate, electric current frequency, electric conductivity of slag skin, and protecting gas flux^[2-4,11-14]. Extended model can be used for ingot quality predictions, such as dendrite arm spacing, macro-segregation, criterion parameters for freckle formation, and also for new technology predictions and evaluations such as current conducting mould, rotating electrode, hollow ingot with multi-electrodes, and ESR process casting with liquid metal^[1,2,14-19]. There is a trend of multi-scale combined simulation^[20] that could realize the prediction and control of solidification structure of ingots.

Other than the suitable slag composition and operating parameters, high quality of consumable electrode is also

Received date: June 14, 2018

Foundation item: National Natural Science Foundation of China (U1708253)

Corresponding author: Wang Lei, Ph. D., Professor, Key Laboratory for Anisotropy and Texture of Materials (Ministry of Education), Northeastern University, Shenyang 110819, P. R. China, Tel: 0086-24-83681685, E-mail: wanglei@mail.neu.edu.cn

Copyright © 2018, Northwest Institute for Nonferrous Metal Research. Published by Elsevier BV. All rights reserved.

critical to obtaining high quality ESR ingots. While, in practice, large or small and deep or shallow holes are frequently formed in the electrode under certain conditions, most likely due to the solidification shrinkage of the ESR electrode made by the up-pouring method in the VIM process. The existence of the shrinkage cavity causes fluctuations in the ESR process, resulting in deterioration of the ESR ingot qualities. In almost all present ESR simulations, a sound, defect-free electrode is assumed. In this work, the specific ESR process of IN718 alloy was selected for simulations considering the different shapes and sizes of electrode shrinkage cavities, a self-developed ESR process model^[21] was used, and the calculated results of physics field distributions, ingot solidification parameters and melting parameters were discussed, so as to provide reference for the quality control of ingot solidification.

1 Mathematical Model Description

1.1 Electromagnetic field model

To simulate the effect of the electrode shrinkage cavity, the magnetic vector potential \vec{A} and scalar potential ϕ equations^[22] were combined to solve the alternating electromagnetic field. Ignoring the induced current caused by fluid flow, the phase or representations of the equations are written as follows:

$$\nabla^2 \vec{A} = \mu \sigma (\mathbf{j} \omega \vec{A} + \nabla \tilde{\phi}) \quad (1)$$

$$\nabla^2 \tilde{\phi} = 0 \quad (2)$$

Here, μ is permeability (H/m), σ is electric conductivity (S/m), ω is angular frequency (rad/s), and \mathbf{j} is $\sqrt{-1}$. Fig.1 shows the geometry domain and corresponding boundaries of the calculation. The calculation domain includes the electrode, slag bath, ingot (including melt pool), and the surrounding zone of air gas. The electrical insulation of the slag skin was assumed to be sufficient; thus, the slag skin and mould zone were not included. Assuming an axisymmetric shape of the shrinkage cavity, as well as the symmetry of the physical process, 2D axisymmetric coordinates were used. Only half of the area was required for calculation, and the symmetry axis was dealt with as a symmetrical boundary. The \vec{A} and $\tilde{\phi}$ each have their own calculation zone and corresponding boundary conditions. For \vec{A} , the calculation zone is the entire region shown in Fig. 1, with the boundary condition of $\partial \vec{A} / \partial n = 0$. Here n represents the normal direction displacement. The calculation of $\tilde{\phi}$ is confined to the conductive zones, also, for the medium interfaces, the condition of continuous electric current in the normal direction is appended. On the top surface of the electrode, $\tilde{\phi}$ is set as the input value $\tilde{\phi}_0$, and on the bottom surface of the ingot, $\tilde{\phi}$ is set to 0. Thus, closed and reasonable solution conditions are constituted.

Based on the calculation results, the Lorentz force and Joule heat are calculated as follows:

$$\vec{J} = -\mathbf{j} \omega \sigma \vec{A} - \sigma \nabla \tilde{\phi}$$

$$\vec{B} = \nabla \times \vec{A}$$

$$\mathbf{F} = \mathbf{J} \times \mathbf{B}$$

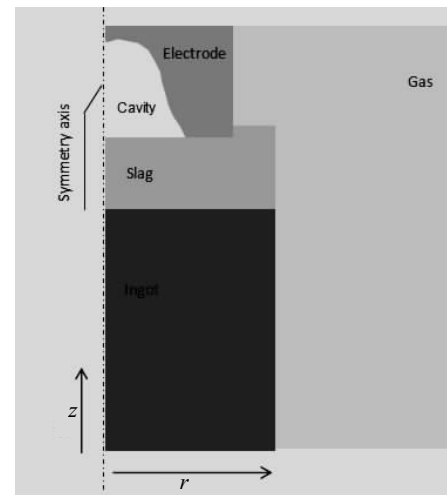


Fig.1 Schematic of geometric domain and boundaries for the electro-magnetic field calculation

$$P = \mathbf{J} \cdot \mathbf{J} / \sigma \quad (3)$$

Here, \mathbf{F} is the Lorentz force (N/m^3), \mathbf{J} is electric current density (A/m^2), \mathbf{B} is magnetic flux density (T), σ is electric conductivity (S/m), P is the Joule heat (W/m^3).

1.2 Fluid flow and heat transfer model

The universal transportation governing equation^[23] is presented as follows:

$$\frac{\partial(\rho\phi)}{\partial t} + \nabla \cdot (\rho \mathbf{u} \phi) = \nabla \cdot (\Gamma \nabla \phi) + S \quad (4)$$

Here, ϕ is calculation variable representing velocity, temperature, concentration, etc; ρ is density (kg/m^3); t is time (s); \mathbf{u} is velocity vector (m/s); Γ is generalized diffusion coefficient ($\text{kg} \cdot (\text{m} \cdot \text{s})^{-1}$); S is source term of each variable equation, and the standard form can be seen in Ref. [23]. In addition, the momentum equation needs appended sources of the Lorentz force and, at the same time, the source of buoyancy should be included for the vertical velocity transportation equation, which is dealt with using the Boussinesq assumption^[23]. The energy equation should consider the source of Joule heat as well as the latent heat of solidification based on the change in volume fraction of solid phase.

Fig.2 provides the geometric domain and corresponding boundaries for the calculation. Similarly, the 2D axisymmetric cylindrical coordinate was chosen. The moving reference was selected to satisfy the consideration of the continuous growth of the ingot and the upward movement of the slag bath. Based on the moving reference and the coordinate with further considerations of ESR process situation and characteristic process variations, all variable boundary conditions and appended source terms of energy equation were determined. In view of the turbulent characteristics of the fluid flow, the standard k - ε model^[23], in association with method of the wall function^[23], was chosen for the calculation. Thus, corresponding

to Eq.(4), ϕ represents 5 variables of u , v , k , ε and T . Here, k is turbulent kinetic energy (m^2/s^2), ε is dissipation rate of k (m^2/s^3), T is temperature ($^{\circ}\text{C}$). The related parameters for the geometry conditions and material properties used in this paper are listed in Table 1.

2 Simulation Results and Discussion

2.1 Model calculation verification

A practical IN718 alloy ESR process was carried out, and the entire process was simulated. Fig.3 shows the calculated

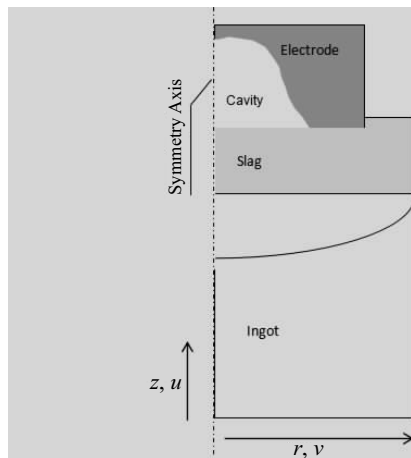


Fig.2 Schematic of geometric domain and boundaries for the fluid flow and heat transfer calculations

Table 1 Parameters of geometric conditions and material properties

Parameters	Value
Radius of electrode/m	0.17
Slag bath height/m	0.123
Immersed depth of electrode in slag pool/m	0.005
Radius of ingot/m	0.215
Radius of gas zone/m	1.175
Electrical conductivity of alloy/ $\text{S}\cdot\text{m}^{-1}$	7.1×10^5
Magnetic permeability of air/ $\text{H}\cdot\text{m}^{-1}$	1.26×10^{-6}
Liquidus temperature of slag/ $^{\circ}\text{C}$	1250
Liquidus temperature of ingot/ $^{\circ}\text{C}$	1350
Solidus temperature of ingot/ $^{\circ}\text{C}$	1205
Latent heat of fusion of electrode/ $\text{J}\cdot\text{kg}^{-1}$	195000
Specific heat capacity of ingot/ $\text{J}\cdot(\text{kg}\cdot\text{K})^{-1}$	750
Specific heat capacity of molten alloy/ $\text{J}\cdot(\text{kg}\cdot\text{K})^{-1}$	750
Density of molten alloy/ $\text{kg}\cdot\text{m}^{-3}$	8000
Density of ingot/ $\text{kg}\cdot\text{m}^{-3}$	8200
Density of molten slag/ $\text{kg}\cdot\text{m}^{-3}$	2750
Thermal conductivity of molten steel/ $\text{W}\cdot(\text{m}\cdot\text{K})^{-1}$	30
Thermal conductivity of ingot/ $\text{W}\cdot(\text{m}\cdot\text{K})^{-1}$	17
Thermal conductivity of molten slag/ $\text{W}\cdot(\text{m}\cdot\text{K})^{-1}$	0.8
Viscosity of molten slag/ $\text{Pa}\cdot\text{s}$	0.03
Viscosity of molten alloy/ $\text{Pa}\cdot\text{s}$	0.007
Thermal expansion coefficient of molten alloy/ K^{-1}	0.0002
Thermal expansion coefficient of molten slag/ K^{-1}	0.0003

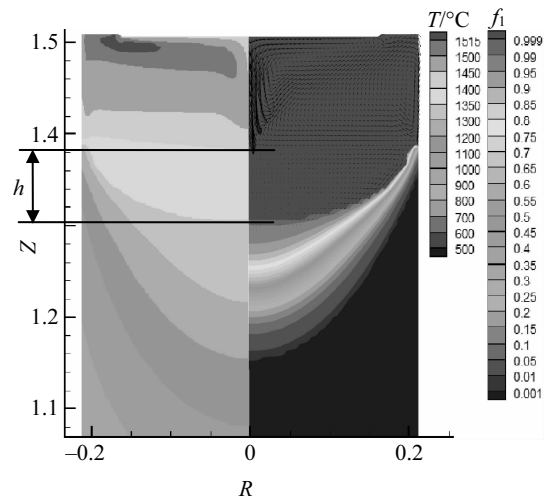


Fig.3 Distribution of flow field, temperature and liquid volume fraction at a certain point during the process

results of the flow field and temperature and liquid phase volume fraction distributions within the slag and ingot zones at a certain time close to the melting end point when the melt rate was controlled at 3 kg/min. It can be seen that the slag temperature is comparatively higher than the temperature of the melt. The high temperature zone in the slag is located near the bottom surface of the electrode, and the highest temperature zone in the slag lies in the vicinity of the bottom corner of the electrode. Overall, the temperature decreases gradually downward along the central axis. The isotherms in the slag pool are approximately horizontal and scattered while turning to vertical and concentrated near the mould wall. When entering the melt pool, the isotherm starts to lean and its angle to the horizontal gradually increases. The angle continuously becomes larger into the mushy zone and then reaches a maximum at the boundary between the mushy zone and the fully solidified ingot zone, where the isotherm of the solidus temperature lies. Beneath the solidus isotherm, the angle becomes smaller in the downward direction with an inverse tendency, and the isotherm becomes flat accordingly.

The molten pool and the mushy zone areas can be defined and distinguished using the contoured line of the liquid volume fraction. The size and shape of the mushy zone are closely concerned with the process control, and are also the basis for extended calculation and model validation. Fig.4 shows the analyzed results of the melt pool profiles near the top of the ESR ingot, where the pool depth value h is marked. Evidently, the calculated melt pool has a similar shape and consistent depth to the experimental one.

Based on the temperature distribution and evolution, the secondary dendrite arm spacing (SDAS) distribution was calculated, as shown in Fig.5. The SDAS shows a gradient distribution in the radial direction, while it has a faint variation along the longitudinal direction except at the upper and

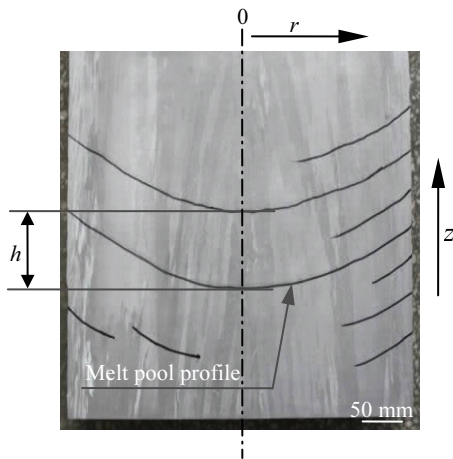


Fig.4 Image of the melt pool shape in axial section of the ingot

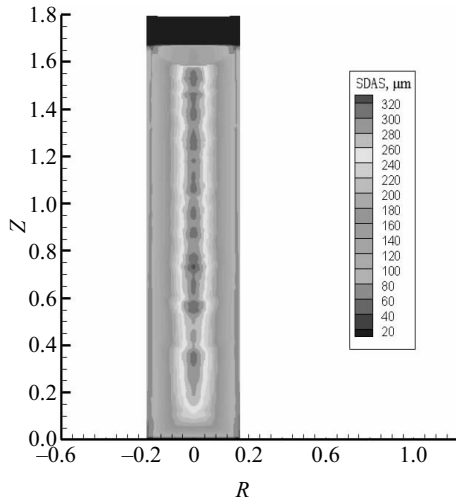


Fig.5 Simulated results of secondary dendrite spacing distribution of solidification quality

bottom part of the ingot.

The SDAS decreases continuously from the ingot center to the outer surface. Fig.6 shows images of the dendrite structure analyzed by sampling along the radial direction of the ingot axial section. Through the comparison between Fig.5 and Fig.6, the magnitude and change tendency of the calculated SDAS in the radial direction coincide with the experimental results fairly well.

2.2 Influence of the shrinkage cavity on electromagnetic field

Four kinds of electrode shrinkage cavities were designed based on practical production, seen in Fig.7a~7d. All cavities were symmetrically designed for ease calculation without the risk of losing generality. The inner shape sizes of the cavities are shown in Fig.7e, and the melt rate was set to 4.0 kg/min; Other parameters are listed in Table 1. Under high temperature

conditions, the materials have the same magnetic conductivity in the atmosphere.

Fig.8 provides the calculated distributions of electric current density J in z direction J_z for the four different shrinkage cavity conditions according to Fig.8a~8d. There is a so-called “skin effect” in alternating electric current situations. As shown in Fig.8a, the magnitude of J_z increases gradually from the inner to the surface of the electrode and the ingot, while it changes much less in the slag with the greater difference in electric conductivity between the slag and the metal. The existence of shrinkage cavity somewhat weakens the skin effect in the electrode and ingot zones, as seen in Fig. 8b to Fig. 8d. The surface current decreases at the upper part of the electrode containing the cavity, and increases at the lower part where the current becomes more uniform with a rather decreased electrode cross-sectional area. For the slag bath, a considerable decrease in current density was observed in the region just beneath the cavity, similarly caused by the changed sectional area between the electrode and the slag. In spite of the deep influence of the cavity, there is no change in the current distributions in the slag and ingot when the longitudinal size of the cavity changes.

Fig.9 shows the calculated distributions of magnetic field intensity amplitude H for the corresponding conditions. H primarily shows that the radial distribution, which is weakest at the center line, increases gradually outward and reaches a maximum at the surface, seen in Fig.9a. H is determined from the electric current distribution according to Ampere’s law. The interval of the isoline in the electrode and the ingot shrinks outward, which is more vivid in the ingot while smaller in the slag, corresponding to the different degrees of skin effect. As the current density changes, H also changes. As shown in Fig.9b~9d, H distributions are quite different from that without the shrinkage cavity (Fig.9a), as their peak values are slightly smaller. H is close to zero within the cavities and slightly higher in the solid part near the top of the shrinkage cavity, as shown in Fig.9b. H is significantly weakened in the local zones of the slag under the cavity, while it changes less at the lower part or near the circumferential surface of the slag pool. Additionally, there is no evident difference in H between the slag and ingot for the cavity of different lengths.

Fig.10 shows the calculated distributions of Joule heat power P and electromagnetic force F in the electrode, showing the slag bath and the upper part of the ingot for the different shrinkage cavity situations. Taking the case of no-shrinkage cavity (Fig.10a) for an example, the Joule heat is generated almost entirely in the slag zone, with the power nearly 4 orders of magnitude larger than that in the electrode and the ingot. P in the slag zone increases as it gradually approaches the bottom of the electrode, reaching a maximum around the corner of the electrode bottom, while it decreases gradually towards the mould, reaching a minimum at the free surface of the slag pool near the mould. F , in all zones, points

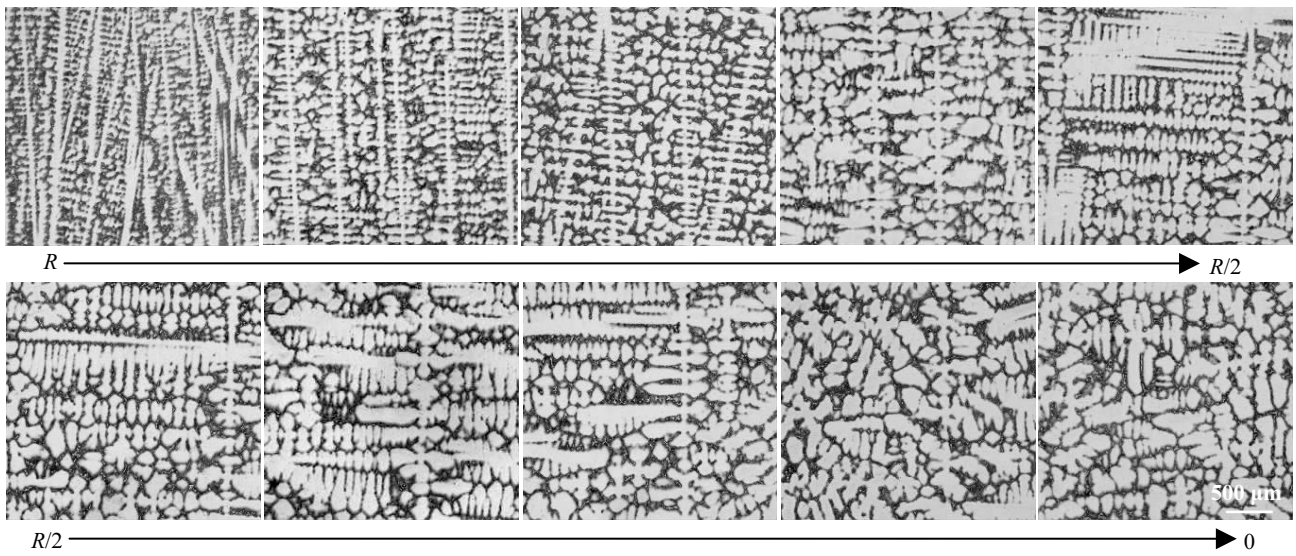


Fig.6 Images of the dendrite structure along the radial direction

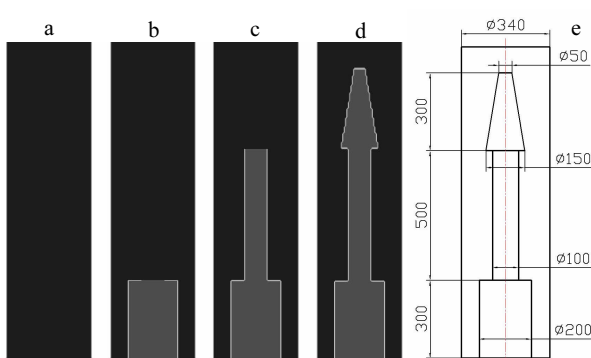


Fig.7 Shapes and dimensions of the designed electrode shrinkage cavity: (a) no shrinkage cavity, (b) cylindrical shrinkage cavity, (c) combination of two different cylindrical shrinkage cavities, (d) combination of two cylindrical and one cone frustum shrinkage cavities, and (e) dimensions of cavity

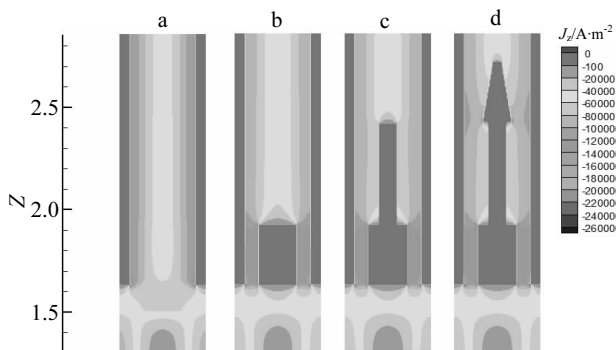


Fig.8 Simulated distributions of electric current density J_z in z direction (displaying domain contains the local air gas zone and the electrode including the cavity, slag and upper part of ingot corresponding to Fig.1; a-d correspond to the different shrinkage cavity situations in Fig.7)

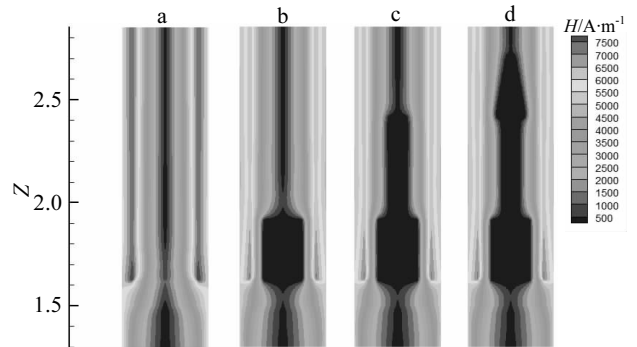


Fig.9 Simulated distributions of magnetic field intensity amplitude H (a-d correspond to the different shrinkage cavity situations in Fig.8)

to the axis center. Except in the local zones near the corner of the electrode bottom, the free surface of the liquid slag and the slag/metal interface, all force directions are nearly horizontal. The magnitude of F decreases from the circumferential boundary to the center and reaches a minimum in the center axis. Compared to F in the electrode and the ingot, the magnitude of F in the slag has a weaker inward damping and a larger effective range, which is a combined effect of B and J according to Eq.(3).

Compared to the case of no-shrinkage cavity, the distributions of P and F in the slag pool are evidently different, as shown in Fig.10b~10d. One additional centralized heat-generating spot appears near the boundary of shrinkage cavity in the slag pool, and the Joule heat of the slag pool zone under the shrinkage cavity is significantly reduced. These effects are caused by changes in the distribution of J due to the existence of the shrinkage cavities. In addition, F nearly decreases to zero near the slag pool surface beneath the

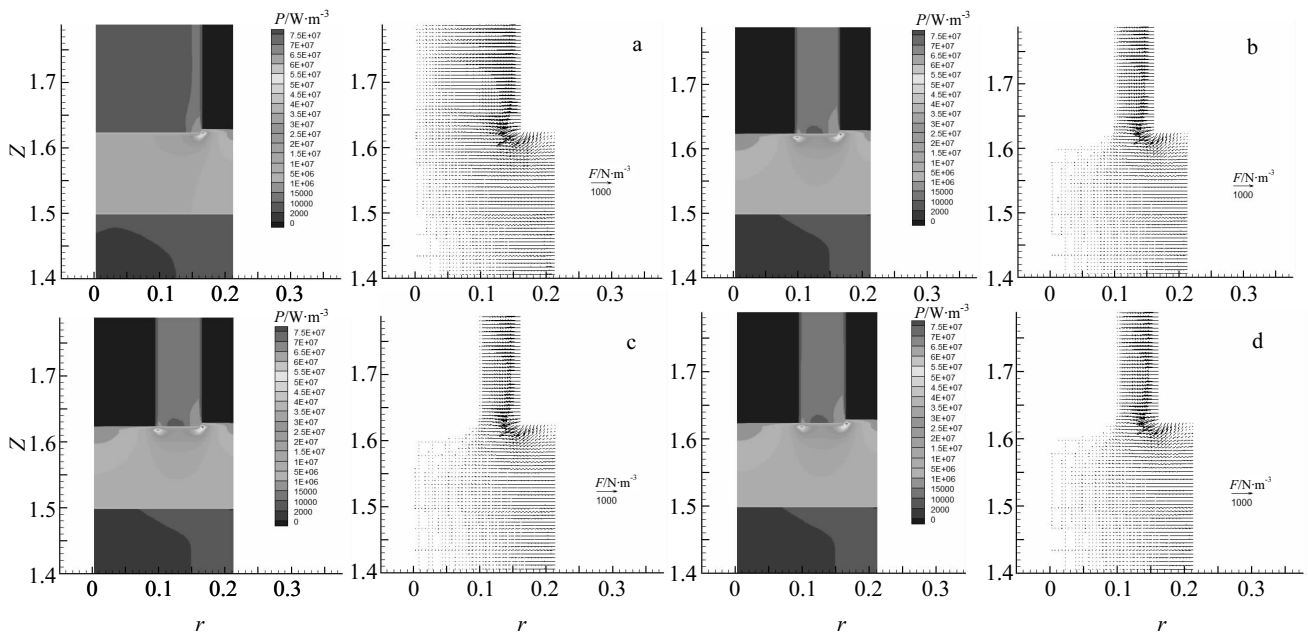


Fig.10 Simulations of Joule heat power P and electromagnetic force F distributions in electrode, slag bath and upper part of the ingot (a~d correspond to the different shrinkage cavity situations in Fig.8)

shrinkage cavity, which is greatly reduced in the lower slag region as well. By comparing Fig.10b~10d, it can be inferred that the axial size of the shrinkage cavity has no obvious influence on the distributions of P and F in the slag pool. The key effect comes from the contact area between the electrode and the slag.

2.3 Influence of shrinkage cavity on the fluid flow and temperature distributions during the ESR process

ESR process simulations were carried out here through multi-field coupling calculation. Since the key role is attributed to the cross-sectional area of the slag/metal interface, the electrode shrinkage cavity can be designed as a simple shape in Fig.7b; the length of the cavity is constant while the radius is designed in 5 different sizes: 0, 0.025, 0.05, 0.075 and 0.1 m. The length of the cavity is set to 0.1 m; thus, even shorter electrodes are sufficiently long. The length of the electrode is set to 0.5 m. The ingot length is 0.7 m here, which is sufficient for the electric magnetic field calculation and heat transfer of present calculation with a specific bottom condition of ingot. The steady-state calculation is selected to approximate the steady-state process. The bottom condition of the ingot is set as heat insulation; thus, the long ingot situation can be modeled with an even shorter ingot. For different radius cavity conditions, a constant melt rate of 4 kg/min is set in view of the commonly used melt rate controlling methods and the anticipated comparable results. The electrode melting rate is determined by both the input power and the heat transfer situations. Similar to the above calculations, the electric conductivity of slag with the same value is introduced here; thus, only one of voltage, current and power is needed.

For present simulations, the voltage is selected as the input parameter, and the value is changed consistently for different cavity conditions owing to different heat transfer conditions. The consistence between the melt rate and the power is the kernel for the reliability of the calculations. This model provides a consistence judgment method based on the heat transfer balance of the electrode^[21]. Other parameters are the same as the above calculation, and additional physical property parameters are required, including density, heat capacity, viscosity, thermal expansion coefficient, liquidus and solidus temperatures, latent heat of solidification, and the blackness coefficient of the slag and the alloy. All values are mainly from references and can be set as inputs through the UI.

Fig.11 shows the simulated distributions of the fluid velocity, temperature and liquid volume fraction for the 5 different cavity conditions. All distributions for different conditions have unified characteristics. Taking the situation of no shrinkage cavity as an example (Fig.11a), there are two main vortexes in the slag pool, one is the counterclockwise flow downward along the central axis caused by the cooling effect attributed to the heating and melting of the electrode, and the other is the clockwise at the mould boundary caused by the mould cooling. In the melt pool, the flow only circulates clockwise downward and inward along the solidified boundary. All flows are determined by the combined effects of electromagnetic force and buoyancy. The flow downward along the central axis in the slag pool is consistent with the magnetic force, while the boundary flows in the slag and melt are opposite to the magnetic force; thus, buoyancy

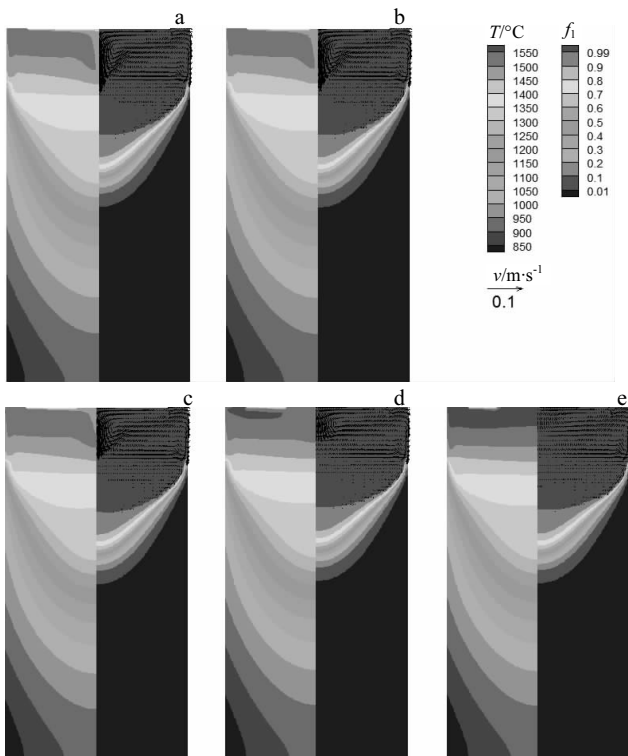


Fig. 11 Simulated distributions of flow velocity vector, temperature and liquid volume fraction for the different shrinkage cavity radii: (a) 0 m, (b) 0.025 m, (c) 0.05 m, (d) 0.075 m, and (e) 0.1 m

plays a dominant role. The temperature isotherms are approximately horizontal in the slag pool, though they change rapidly in the radial direction when approaching the mould boundary and the central axis. The temperature of melt pool is relatively more uniform, as the isotherms are also nearly horizontal and become steep near the solidified boundary. The depth of melt pool and the profile of mushy zone can be determined by the contours of liquid volume fraction in Fig. 8. The isoline 0.99 can represent the boundary of pure liquid, and the isoline 0.01 can represent the boundary of solid. In the middle is the mushy zone. The bottom of melt pool boundary is approximately a circular arc and becomes flat towards the center, while the bottom boundary of the mushy zone is approximately parabolic. In the mushy zone, the isotherm interval decreases downward along the radial axis and the tilt angle (the angle between isotherm and horizontal) gradually increases, which is the result of combined effect of the heat conduction in the ingot, the released solidification latent heat, and the defined cooling conditions. Below the bottom of the mushy zone is the solidified zone, in which the isotherm interval increases, and the isotherm tilt angle decreases along the axial axis. These effects are also caused by the ingot heat conduction and the cooling from the ingot bottom and circumferential surfaces.

There is an increasingly obvious change with the increased radius of the shrinkage cavity, as shown in Fig. 11, which is absolutely located in the slag zone. At first, the comparatively small radius, such as 0.025 m, hardly changes, as can be seen by comparing Fig. 11b with Fig. 11a. As the cavity radius increases to 0.05 m, there is a visible small decrease in center downward flow in the slag pool. With the further increase of the cavity size, the center downward flow in the slag is weakened, and the slag pool temperature increases significantly. For all situations, there is no obvious change in the distributions of velocity, temperature, and liquid volume fraction in the ingot, as well as in the melt pool. This result will be reasonable since the melt rate is the dominant factor in the process. The different statuses in the slag pool are attributed to different power inputs, such as the driving force and heat transfer conditions mentioned below. All the different situations bring the same melt rate; thus, with the present steady-state simulation, no evident change in the melt pool and solidification zones can be seen.

2.4 Influence of the shrinkage cavity on the distribution of ingot solidification parameters

Based on the calculated temperature distributions, the solidification parameters for freckle formation including the local cooling rate (G_{*R}), the local solidification time (LST), the primary and secondary dendrite spacing (PDAS, SDAS), and the criterion of modified Rayleigh number (Ra) can be calculated^[24]. For the present steady-state calculation, only the radial distributions can be obtained. All distributions are displayed in Fig. 8. As shown in Fig. 12a, the G_{*R} value is very small in the ingot center, where it gradually increases outward at an increasing rate in the radial direction until reaching the ingot surface. When close to the surface, it rises sharply and obtains the maximum on the surface. It can also be seen that G_{*R} is obviously unaffected by the radius change of the shrinkage cavity. As shown in Fig. 12b, LST is the highest at the center where it gradually decreases outward from the middle radius to the surface of the ingot in an approximately linear manner. Additionally, the variation in the shrinkage cavity size has the minimal influence on the LST. Fig. 12c and Fig. 12d show PDAS and SDAS distributions in the corresponding situations. Both figures show an approximately linear decrease outward. Again, there are few differences in all distributions of PDAS and SDAS for the different cavity size situations. The modified Rayleigh number Ra ^[24] is a mathematical criterion used to evaluate the possibility of freckle formation. When Ra exceeds the critical value Ra^* , freckles tend to form with a high possibility; otherwise, no freckles would form. It has been reported that freckles form during solidification process rather than at the solidification front^[24]. Therefore, two modified Ra numbers corresponding to different solid fractions (f_s) of 0.5 and 0.8 are selected as the criteria. Fig. 12e and 12f show the radial distributions of the ratios of the calculated Ra to the critical values of Ra_1/Ra^* and

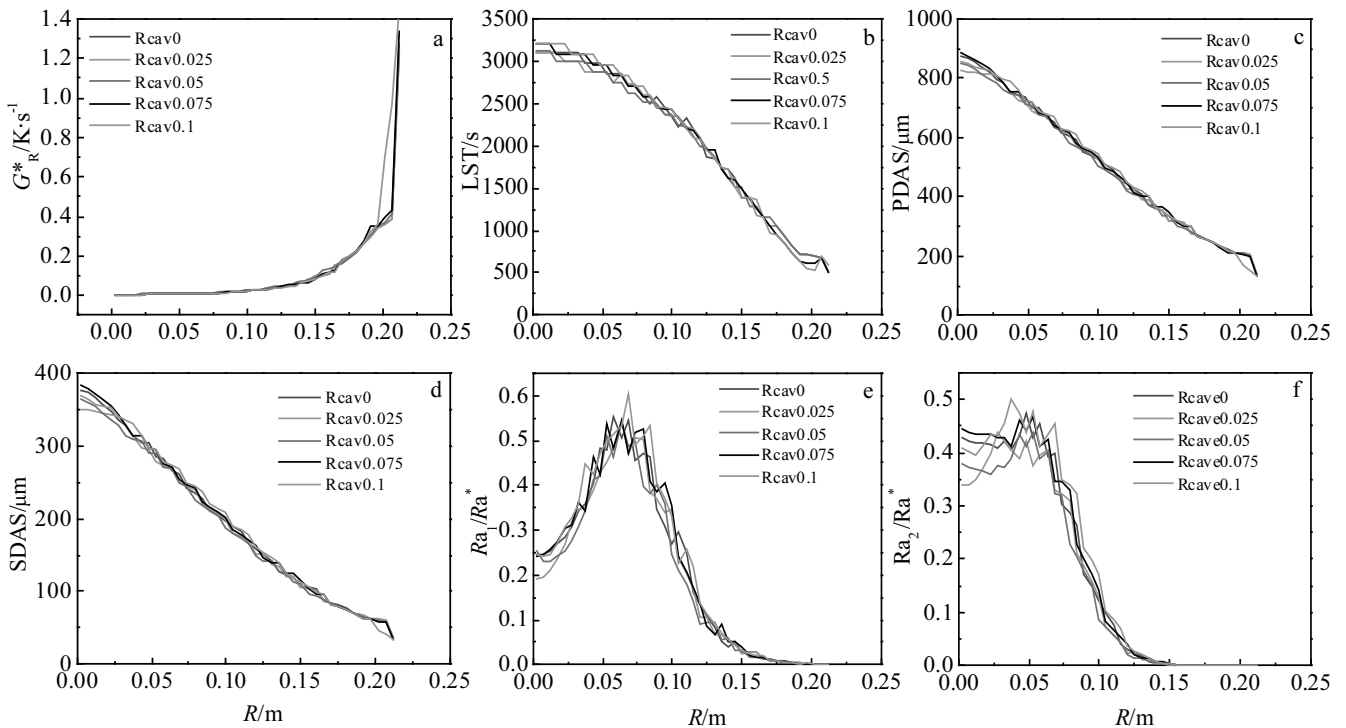


Fig.12 Calculated distributions of the solidification parameters along the ingot radius under the conditions of different shrinkage cavity sizes: (a) G^*_R , (b) LST, (c) PDAS, (d) SDAS, (e) Ra_1/Ra^* ($f_s=0.5$), and (f) Ra_2/Ra^* ($f_s=0.8$)

Ra_2/Ra^* , respectively. Ra_1/Ra^* is the maximum at the position of nearly 1/3 radius, where it gradually decreases inward or outward. Ra_2/Ra^* shows a similar trend, but it is higher than Ra_1/Ra^* in the ingot center. The peak values of Ra_1/Ra^* and Ra_2/Ra^* are both less than 1, which means that the possibility of freckles formation is minimal at this melt rate. In addition, the values of these two parameters vary merely in a small range with the increase of shrinkage cavity radius up to 0.1 m.

2.5 Influence of shrinkage cavity on the melting parameters

Additional results of melting parameters including the power, voltage, and current can be determined from the simulation corresponding to a specific melt rate and melting situation. The specific melting situation particularly refers to the different shrinkage cavities in this paper. A specific practical process using an electrode containing a shrinkage cavity is selected here for a similar systematic calculation aiming at the designed different radius cavity conditions. Thus, the calculated melting parameters can be compared with the measured values. All the geometric and physical property parameters are the same as the calculations above, except the melting parameters. The melt rate is set as the practical value. The slag electric conductivity is introduced, and only one melting parameter is required. Here, the power is set to the input parameter, which can be adjusted as mentioned above. Thus, the consistence between the power and the melt rate can be attained. Two other parameters of the voltage and the

electric current can be deduced based on the results of electric magnetic field calculation. From a consistence point of view, no difference in results will be brought for different choices of the input melting parameter, since all the parameters are uniquely determined for a specific melt rate and melting situation.

Fig.13 gives simulated melting parameters for current and power inputs in the ESR processes with different sizes of shrinkage cavities. It can be seen that there are nonlinear relationships between the radius of shrinkage cavity and the two melting parameters. The changes in input power and current are negligible if the radius of the electrode shrinkage cavity is less than 0.025 m. As the cavity size becomes larger, the current decreases gradually in a small range, which is attributed to the increased electric resistance caused by the decrease in the contact area between electrode and slag, while the power varies minimally up to a cavity size of 0.05 m. When the cavity size is larger than 0.05 m, both parameters quickly transit into a rapid increase with the increase of the cavity size. At a cavity radius of 0.1 m, the consumed power increases by 19.4% and the current increases by 4.9% compared with the case without the cavity.

Fig.14 shows the actual ESR melting power, current and melt rate curves using an electrode containing a shrinkage cavity. The opening shrinkage diameter is approximately 200 mm, and its depth is approximately 700 mm. For most of the

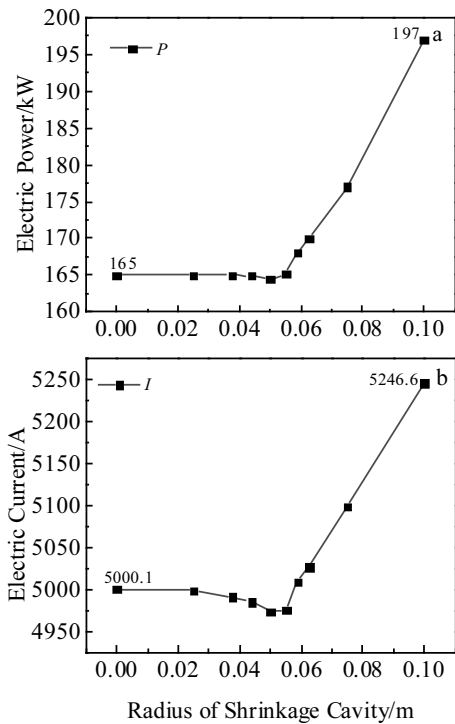


Fig.13 Simulated melting parameters for various sizes of shrinkage cavities in the electrode: (a) power and (b) current

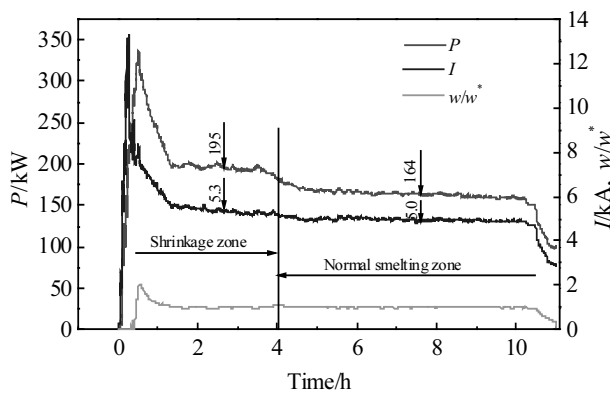


Fig.14 Practical power, current, and melt rate curves for ESR process when using electrodes with shrinkage cavities (w is the melt rate, and w^* is a reference value)

time except the melting start and hot topping phase, the ESR melt rate remains nearly constant. When the shrinkage cavity is melted at the constant melt rate, the actual power is approximately 195 kW, and the corresponding current is approximately 5.3 kA. These two values can be compared with the calculated melting parameters of 197 kW and 5.25 kA, respectively, when the shrinkage radius is 0.1 m (Fig. 14). With the progression of the melting process, the shrinkage zone is gradually melted away, and the power and current gradually return to normal melting values. For the normal

smelting zone, the constant melt phase corresponds to the no-shrinkage calculation. In this phase, the actual power and current values are approximately 164 kW and 5.0 kA, where the corresponding calculated results are 165 kW and 5.0 kA, respectively, as seen in Fig.14. The calculated melting parameters are very close to the measured values at a specific melt rate with simultaneously the consistent sizes of the shrinkage.

2.6 Discussion

Simulations point out that there is a critical value of the shrinkage cavity size for the judgment of the evident effect brought by ESR system. Below this value, almost no effect is seen, while, above this value, an increasingly evident effect appears with the increasing size. This phenomenon is attributed to the existence of a certain degree of "skin effect" under alternating current conditions. The skin effect renders the electrode to have a confined electric-conducting sectional area, i.e., a hollow conductor. Thus, when the cavity does not match the region of the hollow area, its influence on the distributions of electromagnetic force and Joule heat in the slag is small or even negligible. However, once its size exceeds the critical value, its influence becomes increasingly evident. Additionally, the cavity is generally located at the bottom center of the electrode where the slag pool surface temperature is relatively lower than other slag areas adjacent to the electrode bottom (Fig.8), which means that the center of the electrode bottom surface is not a crucial heat transfer area. Therefore, a cavity with a relatively small size has no notable influence on the flow and heat transfer in the slag pool.

In spite of the evident influence on the slag bath flow and temperature distribution brought by the shrinkage cavity, it has no obvious effects on the ingot solidification according to the above simulation results. This result does not indicate a negligible influence of the shrinkage cavity on the ingot quality. The calculated small effect of the shrinkage cavity is due to the steady-state assumption with a constant melt rate, and since the melt rate is the predominant factor, this result is reasonable. Nevertheless, there is a profoundly deep effect of the shrinkage cavity as revealed by the calculation results of the changed melting parameters. To achieve a prescribed melt rate, the input power, current and voltage will be adjusted drastically and constantly when melting through the cavity zones in the electrodes and even regions above and behind the cavity. This effect makes it difficult to maintain the stability of the system, leading to drastic fluctuations in the melting parameters and system status, thus deteriorating the ingot quality. To obtain a stable and high precision control of all remelting parameters, the radius of electrode shrinkage cavity should be controlled within 0.05 m and, if possible, less than 0.025 m. Then its influence of the shrinkage cavity can be neglected.

The critical size of the electrode shrinkage cavity has been deduced in this study, and it can be served as a reference for

judging the cavity-containing electrode in production. This value is suitable for the specific size magnitude or approximate size conditions of the electrodes and ingots in this paper.

Nevertheless, it must be emphasized that, in order to ensure process stability, uncertain factors should be avoided as much as possible. Therefore, the key is to take measures to minimize the size of the shrinkage cavity, such as reducing the VIM electrode casting temperature and pouring speed, increasing the baking temperature of electrode moulds, and using insulating riser.

3 Conclusions

1) A self-developed ESR simulation model based on a multiple physics field-coupled calculation, including the electromagnetic field, fluid flow, and heat transfer, was introduced for the simulation. The specific IN718 alloy ESR process was selected for this study.

2) The existence of the cavity brings a significant change in the distributions of magnetic field intensity and current density in the electrode and slag bath, as well as Joule heat and electromagnetic force, but with only small changes in the ingot. In spite of the significant change caused by the cavity, there is no obvious difference in all these distributions in the slag bath and ingot between the designed cavity existence situations. The key factor is attributed to the contacting area between the electrode and the slag, while the longitudinal size of the cavity is negligible.

3) At a radius value of 0.05 m or more, an increasingly evident influence on the slag zone appears via a weakened center downward flow and increased temperature, whereas, there is a small change below the critical value. Despite the increased effect on the slag bath, there is no obvious influence on the ingot including the melt pool and mush zone for the constant melt rate process.

4) A critical value for a cavity radius of approximately 0.05 m was obtained to judge the evident change in melting parameters. Below the critical value, faint or even no change of the parameters appears. However, above this value, the parameters soon turn into high-speed changes in an approximately linear manner. From the standpoint of process control stability, the radius of electrode shrinkage cavity should be controlled below 0.05 m for the ESR ingot with a diameter of 430 mm.

References

- Morales B H, Mitchel A. *Ironmaking Steelmaking*[J], 1999, 26(6): 423
- Fezi K, Matthew Y J, Krane J M. *Metallurgical and Materials Transactions B*[J], 2015, 46(2): 766
- Kelkar K M, Patankar S V, Mitchell A. *International Symposium on 'Liquid Metal Processing & Casting'*[C]. Wiley- TMS, 2005: 137
- Weber V, Jardy A, Dussoubs B et al. *Metallurgical and Materials Transactions B*[J], 2009, 40(3): 271
- Wei J H, Ren Y L. *Acta Metallurgica Sinica*[J], 1995, 31(2): 51 (in Chinese)
- Geng M P, Sun D X. *Process Control and Simulation in Electroslag Casting*[M]. Beijing: Metallurgical Industry Press, 2008: 21 (in Chinese)
- Li B K, Wang B, Tsukihashi F. *Metallurgical and Materials Transactions B*[J], 2014, 45(3): 1122
- Wang Q, He Z, Li B K et al. *Metallurgical and Materials Transactions B*[J], 2014, 45(6): 2425
- Kharicha A, Mackenbrock A, Ludwig A et al. *International Symposium on 'Liquid Metal Processing and Casting'*[C]. Wiley-TMS, 2007: 107
- Bai H J, Li Y, Li B K. *Special Steel*[J], 2008, 29(1): 7 (in Chinese)
- Sibaki E K, Kharicha A, Wu M et al. *Proceedings of the 2013 International Symposium on 'Liquid Metal Processing and Casting'* [C]. Wiley-TMS, 2013: 13
- Hugo M, Jardy A, Dussoubs B J et al. *Journal for Manufacturing Science & Production*[J], 2015, 15(1): 79
- Yan C, Li Y, Ma B Y et al. *Materials Research Innovations*[J], 2015, 19(S1): 62
- Jardy A, Ablitzer D. *Materials Science and Technology*[J], 2009, 25(2): 163
- Liu F B, Zang X M, Jiang Z H et al. *International Journal of Minerals, Metallurgy and Materials*[J], 2012, 19(4): 303
- Wang Q, Gosselin L, Li B K. *ISIJ International*[J], 2014, 54(12): 2821
- Liu F B, Jiang Z H, Li H B et al. *Ironmaking and Steelmaking*[J], 2014, 41(10): 791
- Dong Y W, Zheng L C, Jiang Z H. *Ironmaking and Steelmaking* [J], 2013, 40(2): 153
- Dong Y W, Jiang Z H, Medova L et al. *Steel Research International*[J], 2013, 84(10): 1011
- Nastac L, Sundarraj S, Yu K et al. *JOM*[J], 1998, 50(3): 30
- Li Q, Wang Z X, Xie S Y. *Acta Metallurgica Sinica*[J], 2017: 53(4), 494 (in Chinese)
- Xie D X, Yao Y Y, Bai B D et al. *The Finite Element Analysis of Three-dimensional Eddy Current Field*[M]. Beijing: China Machine Press, 2001: 12 (in Chinese)
- Tao W Q. *Numerical Heat Transfer, Second Edition*[M]. Xi'an: Xi'an Jiaotong University Press, 2001: 5, 351, 242, 347, 353 (in Chinese)
- Auburtin P, Wang T, Cockcroft S L et al. *Metallurgical and Materials Transactions B*[J], 2000, 31(4): 805

数值模拟电极缩孔对 IN718 合金电渣重熔过程的影响

王资兴^{1,2}, 李青², 王磊¹

(1. 东北大学 材料各向异性与织构教育部重点实验室, 辽宁 沈阳 110819)

(2. 宝山钢铁股份有限公司研究院, 上海 201900)

摘要: 利用自主开发的 ESR 过程仿真软件, 针对直径 430 mm 的 IN718 合金铸锭, 通过设计不同形状尺寸的电极缩孔, 进行电渣重熔过程的数值模拟计算和分析。结果表明, 基于电磁场、流场和温度场等多物理场耦合计算自主开发的 ESR 数学模型及仿真软件, 可以用于 ESR 冶炼全过程数值模拟, 模型计算的熔池形状和深度、二次枝晶臂间距分布规律与实际剖锭分析结果接近。电极中存在缩孔改变了电极与渣池的接触面积, 从而显著影响渣池的焦耳热和电磁力分布, 而缩孔沿电极轴向尺寸的变化对二者分布的影响则很小。在恒熔速条件下, 当缩孔半径小于 0.025 m 时, 缩孔对熔炼过程几乎没有影响; 当缩孔尺寸继续增大时, 渣池温度场和流场发生明显改变, 渣池温度逐步升高, 中心向下流速相对减弱; 电极缩孔尺寸变化对熔池温度场及两相区尺寸影响不明显。缩孔半径尺寸对电流和功率等熔炼参数的影响呈非线性关系, 临界变化值约为 0.05 m, 当缩孔半径低于临界值时, 对电流和功率等影响较小; 高于临界值时, 随着缩孔半径增加, 电流和功率显著增加, 并且增速不断加快。从工艺过程控制稳定性角度而言, 该尺寸电极缩孔半径应控制在 0.05 m 以下。

关键词: 电渣重熔; 数值模拟; 电极缩孔

作者简介: 王资兴, 男, 1981 年生, 博士生, 高级工程师, 宝山钢铁股份有限公司研究院, 上海 201900, 电话: 021-26032450, E-mail: wangzixing@baosteel.com